Polymer Journal (2019) 51:511–521
https://doi.org/10.1038/s41428-018-0166-z

ORIGINAL ARTICLE

Soft, conductive nanocomposites based on ionic liquids/carbon nanotubes for 3D printing of flexible electronic devices

Kumkum Ahmed[1] · Masaru Kawakami[1,2] · Ajit Khosla[1] · Hidemitsu Furukawa[1,2]

Received: 9 October 2018 / Revised: 3 December 2018 / Accepted: 5 December 2018 / Published online: 17 January 2019

Abstract

In this work, we present the preparation, characterization, and 3D printing of highly conductive, soft, and functional nanocomposite polymers. The prepared nanocomposite is a polymeric system that consists of poly (ionic liquid) (PIL), polymethylmethacrylate (PMMA), and multiwalled carbon nanotubes (MWCNTs) as fillers and an ionic liquid (IL) that acts as a plasticizer and dopant for the MWCNTs. The nanocomposites exhibited variable mechanical (strain at break: 50–250%) and conductive properties depending on their composition, and the highest conductivity of 520 Sm^{-1} was attained with 15 wt.% MWCNT loading owing to the well-defined morphology of the MWCNTs revealed by SEM. The thermal properties of the nanocomposites were measured by thermogravimetric analysis (TGA), differential scanning calorimetry (DSC), and dynamic mechanical analysis (DMA). The results revealed high thermal stability up to 340 °C regardless of the composition and a variable transition temperature dependent on the MWCNT, IL, and polymeric contents. Finally, the conditions for 3D printing were optimized, and as a proof of concept, we demonstrated the fabrication of a flexible, 3D-printed circuit, which can be bent and twisted without damaging the circuit.

Introduction

The use of 3D-printing technology in fabricating new materials, such as polymers, gels, composites, and metals, is growing rapidly owing to considerable technological amendments in engineering [1–9]. Conductive nanocomposites composed of conductive fillers (e.g., carbon nanotubes/fibers, graphene, and metallic nanowires) are one of the most researched topics in 3D-printing technology due to their potential applications in the fields of robotics, tactile sensors, and microelectrochemical systems [1, 10–12]. Although metal works best in the abovementioned applications, metals are very expensive and difficult to 3D print because of their high melting temperature and rigidity. The development of carbon-based nanocomposites with high conductivity and flexibility for 3D printing is not a very facile task to accomplish. Researchers have fabricated rigid nanocomposite structures combining carbon filler/polymer composites, such as carbon black/polycaprolactone, graphene/PLA feeding filaments by fused deposition modeling (FDM) or carbon nanotube (CNT)/PLA composites by solvent casting and UV-assisted 3D printing [13–15]. 3D printing of various conductive nanocomposites, such as nanocomposite inks, carbon conductive grease and silicone/silver nanocomposites for tactile, and strain sensing, has been reported [10, 11]. However, 3D printing of silicone-based nanocomposites requires sophisticated 3D-printing systems.

In this work, we present a facile approach for developing 3D-printable, soft, and conductive nanocomposites via a simple fused filament fabrication (FFF) printing technique. We used quaternary ammonium cationic IL-based polymeric systems and MWCNTs, because ILs have been proven to effectively disperse CNTs in polymer matrices and create soft functional materials [16–21]. ILs are salts with melting points below 100 °C and have attracted remarkable interest due to

Supplementary information The online version of this article (https://doi.org/10.1038/s41428-018-0166-z) contains supplementary material, which is available to authorized users.

✉ Hidemitsu Furukawa
furukawa@yz.yamagata-u.ac.jp

[1] Department of Mechanical System Science, Graduate School of Science and Engineering, Yamagata University, Jonan 4-3-16, Yonezawa, Yamagata 992-8510, Japan

[2] Life-3D Printing Innovation Center (LPIC), Yamagata University, 4-3-16 Jonan, Yonezawa 992-8510, Japan

their unique properties, such as nonvolatility, wide electrochemical window, high thermal stability, and high ionic conductivity [22, 23]. CNTs dispersed in IL form composites known as "Bucky gels" [16] that are well-known combinations used as electrode materials for different electrochemical devices and sensors due to their low operating voltage, long lifespan in air, and minimal weight [24–27]. ILs have also been found to have multifunctional roles as a compatibilizer, plasticizer, and processing aid in melt-blended polymer-MWCNT nanocomposites [21]. Polymers derived from ILs, commonly known as poly(ionic liquid) (PIL), have also been reported for a variety of applications [27, 28]. The use of a PIL along with CNTs as a filler to develop new functional materials is still in the initial stage of research. To date, only a few studies have proposed the use of PIL-CNT combinations as wrapping agents for CNTs [20], stabilizers [27], end-functionalized CNT dispersions [29], or additives [29, 30]. Although both ILs and PILs have been individually used with CNTs to develop nanocomposites, to date, no work has focused on the preparation of 3D-printable nanocomposites utilizing ILs/PILs and CNTs. Due to the poor mechanical properties [30] and brittle nature of PILs, PIL-CNT composites do not have practical application value for 3D printing, because 3D printing via the FFF method requires a material with a suitable mechanical strength and ductility. Here, we demonstrate that combining a compatible polymer with a PIL can result in nanocomposites with variable mechanical stiffness and ductility. Therefore, the focus of our work is to develop new nanocomposites by combining IL, PIL, PMMA, and MWCNTs and discuss their mechanical, conductive, thermal, and morphological properties along with a demonstration of 3D fabrication of flexible circuits.

Experimental section

Materials

IL monomer *N,N*-diethyl-*N*-(2-mthacryloylethyl)-*N*-methylammonium bis(trifluoromethylsulfonyl) imide (DEMM-TFSI) and IL *N*-diethyl-*N*-methyl-*N*-(2-methoxyethyl)ammonium bis(trifluoromethylsulfonyl)imide (DEME-TFSI) were purchased from Kanto Chemicals and used as received. MWCNTs were received from Nanocyl, named NC7000™. PMMA (specific gravity of 1.188) was received from Fujifilm Wako Pure Chemical Corporation, and the solvents acetone and acetonitrile (GC 99.5% mass/mass) were received from Wako Chemicals and used without any further purification.

Preparation methods

The chemical structures of the ILs and the synthesis processes of the PIL and nanocomposites are shown in Fig. 1(a–d). The entire process for the preparation of the nanocomposites consists of the following steps: synthesis of the PIL PDEMM-TFSI from the monomeric IL DEMM TFSI, dissolving the PIL, PMMA, and IL in acetone, and mixing the MWCNTs with polymeric solution (stirring and grinding with an agate mortar), followed by drying to obtain the final nanocomposites. The polymer PMMA was selected due to its suitable compatibility with the IL and PIL, good mechanical strength (suitable for 3D printability), amorphous nature (to avoid complex molecular structures when combined with IL/PIL), and thermoplastic properties. The PIL PDEMM-TFSI was synthesized by a free radical polymerization process using the thermal initiator AIBN. The monomer, DEMM TFSI, was first dissolved in acetonitrile, followed by addition of the initiator and heating at 70 °C for 6–7 h. To completely remove the solvent, the mixture was further dried under vacuum for another 12–15 h at room temperature (r.t.) to obtain the final product PDEMM-TFSI. No further purification steps were performed, and the PIL was used as synthesized and kept in a glove box for storage. To prepare the nanocomposites, the synthesized PIL and commercial-grade PMMA (1:1 weight ratio or 25 wt.% each, unless otherwise mentioned) were dissolved in acetone by a magnetic stirrer until the polymers were completely melted. In the next step, IL DEME-TFSI was added according to the required quantity depending on the MWCNT content. MWCNT contents of various wt.%, e.g., 0.5. 5, 7, 8, 10, and 15, were added to the polymer mixtures and stirred overnight to ensure good dispersion of MWCNTs in the polymer solution. The nanocomposite compositions are listed in Table 1. Before transferring the mixture for the drying process, the mixtures were ground on an agate mortar for 30 min, cast on a teflon vessel in a drying oven at 60 °C for 12 h, followed by drying under reduced pressure at 30 °C in a vacuum oven for 4–6 h. A "Noztec Pro Pellet and powder filament extruder" with a 1.75 mm nozzle diameter was used to make filaments. The prepared composites were crushed using a commercial grinder and passed through the filament extruder at a temperature of 200 °C at the default speed of the extruder, ~2.5 m per minute. This process was performed twice to ensure better mechanical homogeneity and enhanced conductivity in the filament form. During the whole process, the temperature of the extruder was set at 200 °C. Before changing the composition, the extruder was cleaned every time by passing polypropylene through, and the filaments produced in the first few minutes were discarded.

Characterization methods

The molecular weight (MW) of PIL was determined using a Horiba Nanopartica SZ-100 instrument in static light-scattering mode. A Debye plot was created by measuring the scattered light at a single angle (90 °) for multiple

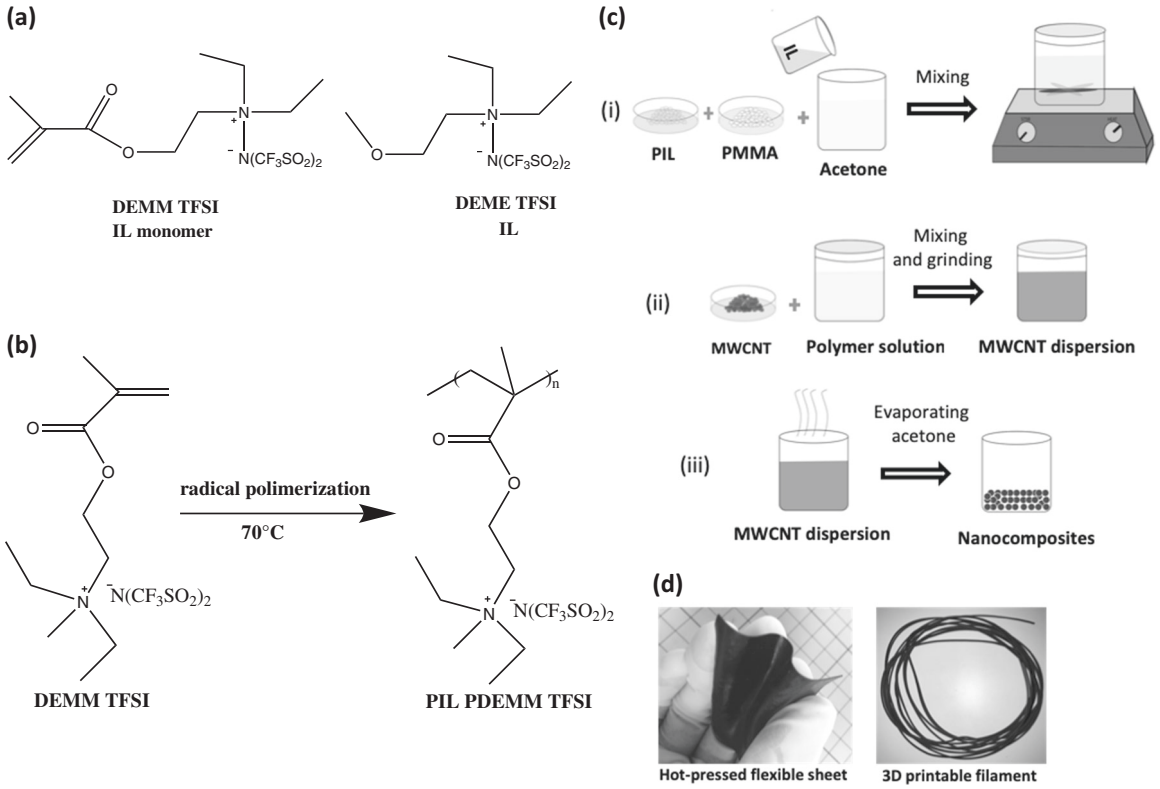

Fig. 1 **a** Chemical structure of the IL and the monomeric IL, **b** synthesis of the PIL, **c** schematic step by step preparation process of PIL-MWCNT nanocomposites representing mixing of PIL, IL, PMMA, and MWCNT dispersion followed by drying, **d** flexible sheet and filament

Table 1 Composition of each component in the nanocomposites

Sample name	PIL-PMMA ratio (wt.-wt.%)	IL wt.%	MWCNTs wt.%
PIL-PMMA control	1:1 (50–50 wt.%)	50	0
MWCNT 5 wt.%, IL45	1:1 (25–25 wt.%)	45	5
MWCNT 7 wt.%, IL43	1:1 (25–25 wt.%)	43	7
MWCNT 8 wt.%, IL42	1:1 (25–25 wt.%)	42	8
MWCNT 8 wt.%, IL22	1:1 (35–35 wt.%)	22	8
MWCNT 10 wt.%, IL40	1:1 (25–25 wt.%)	40	10
MWCNT 15 wt.%, IL35	1:1 (25–25 wt.%)	35	15

sample concentrations. The intercept of the Debye plot was used to determine the MW. The Fourier transform infrared (FTIR) spectra of the IL, PIL, PMMA, MWCNTs, and nanocomposites were recorded at r.t. with a Jasco FTIR 460 plus instrument. An X-ray diffraction study was carried out with a Rigaku Ultima IV X-ray (Japan) in the 2θ range of 5–60 ° with a Cu X-ray tube. The tube potential was 20 kV, and the tube current was 2 mA. The samples for XRD measurement were prepared by hot pressing the PIL, PMMA, and nanocomposites, and the sheet (thickness: 1 mm) of each sample was positioned on the sample holder. The holder was placed in the measuring chamber, and data were recorded. Hot pressing was performed on an As-1 HC300–01 machine to prepare the samples for mechanical testing. Gelatinous powder-type composite material was pressed at 140 °C under an applied pressure up to 5 MPa and cooled to r.t. using a 1–2-mm spacer. These sheets were used for conductive and mechanical characterizations. Tensile measurements were carried out with the ORIENTEC testing machine (model STA-1150) at r.t. A dumbbell-shaped specimen (K6251–8) was used to cut the samples from the sheets of the nanocomposites. The size of the composite sheets was ~50 mm long, 4 mm wide, and 0.4–0.6 mm thick, and the crosshead speed during the tensile tests was 50 mm/min. The DC conductivity of the composites was measured using a resistivity processor Sigma 5+ (NPS, INC) four-point probe at r.t. Scanning electron microscopy (SEM) analysis was performed on a

JSM 7600FA scanning electron microscope to observe the morphological behavior of the nanocomposite film and filament. Thermogravimetric (TG) measurements of the samples were conducted using open Al pans on a Seiko Instruments thermogravimetry/differential thermal analyser Seiko Exstar 6000 (TG-DTA 6300) from r.t. to 550 °C at a heating rate of 10 °C/min under a N_2 flow of 100 ml/min. Differential scanning calorimetry (DSC) was performed using a Seiko EXSTAR 6200 DSC analyser under a continuous N2 gas flow with a flow rate of 100 ml/min and a heating rate of 10 °C/min. Dynamic mechanical analysis (DMA) was performed on polymer films (20 mm in length, 5 mm in width, and 0.3 mm in thickness) under a N_2 environment using a Seiko Exstar 6000 (DMS 6100) DMA in tensile mode at a frequency of 10 Hz with a heating rate of 2 °C/min in the temperature range from −50 to 150 °C.

Results and discussion

Material design for 3D-printable nanocomposites

Conventional methods of material design for 3D printing mainly concentrate on the base polymer matrix (thermoplastics or resins), wherein a functional material or filler is added to achieve 3D-printable thermoplastics with new functionality. For example, in the case of the FFF printing process, ABS and PLA are the most common base matrices, wherein conductive or magnetic fillers are added to introduce new functionalities. As a result, very few combinations of materials with similar ranges of physical properties are achieved. In contrast, we designed a composite in which the materials responsible for creating new functionality (softness and conductivity) were initially chosen, followed by adding a suitable matrix polymer to adjust their mechanical properties. Our main objective was to obtain a material with good mechanical ductility, enhanced conductivity, and facile processability. MWCNTs have two main functions within nanocomposites: contribute to the electrical conductivity and create mechanical bridging within the polymeric phase. Due to the presence of a large π-electron surface in CNTs, they are considered to form either cation-π interactions or interact via weak van der Waals forces with the ions of ILs [31–33]. In this case, we considered that the MWCNTs and the ionic groups of the IL and PIL are connected via such interactions, which mainly contribute to debundling of the nanotubes. PMMA acts as a plasticizer and chain stiffener within the MWCNT-polymeric IL cluster, and the IL mainly creates a suitable medium to promote dispersion of MWCNTs within the polymeric network (Fig. 2). The PIL contributes to the flexibility of the nanocomposite when present at a critical composition, and a well-organized homogeneous composite was developed

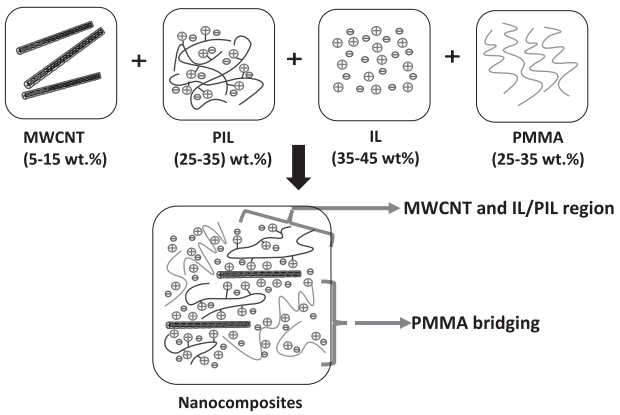

Fig. 2 Formation mechanism of soft, conductive nanocomposites

(Supplementary Information). The MW of the PIL was 171,000 $gmol^{-1}$, as determined by the SLS technique. The MW of the PIL might influence the mechanical properties of the nanocomposites. Therefore, PILs with other MWs will require critical adjustment of the composition to achieve soft nanocomposites. Our future work will discuss the effect of the MW of the PIL on the properties of nanocomposites in detail. At a high MWCNT content (15 wt.%), the PIL and IL contents present are lower than those present with a low MWCNT content (5 and 8 wt.%), consequently resulting in aggregation of more MWCNTs within a small volume and forming somewhat less flexible nanocomposites, as evidenced in the mechanical properties section. Therefore, we can conclude that choosing an appropriate composition of the constituents plays a critical role in defining the properties of the nanocomposites.

Chemical and structural analyses

The FTIR spectra of the IL monomer and synthesized PIL, P(DEMM TFSI), are presented in Fig. 3(a). In the spectrum of DEMM TFSI, the appearance of the C = O stretching vibration band at 1724 cm^{-1} and the C = C stretching band at 1638 cm^{-1} can be attributed to the methacrylate group in the monomer, whereas in the spectrum of PIL, the disappearance of the C = C stretching band near 1638 cm^{-1} confirms the successful polymerization of the monomer. In the PIL spectrum, the C = O stretching vibration band shifts to 1730 cm^{-1}. Other major peaks near 515, 571 cm^{-1} (ascribed to the asymmetrical bending vibration of the $–CF_3$ group of the TFSI− anion) [34, 35], 617 cm^{-1} (deformation mode of the SO_2 group of the TFSI− anion [33, 34], 1056 cm^{-1} (asymmetrical S–N–S stretching mode of the TFSI− anion) [34–36], 1351 cm^{-1} (stretching vibration of the S = O bond of the TFSI− anion) [35, 37], and 1481 cm^{-1} (C–H bending of the methyl group) are observed for the monomer. After polymerization, the abovementioned peak positions became 514, 571, 616,

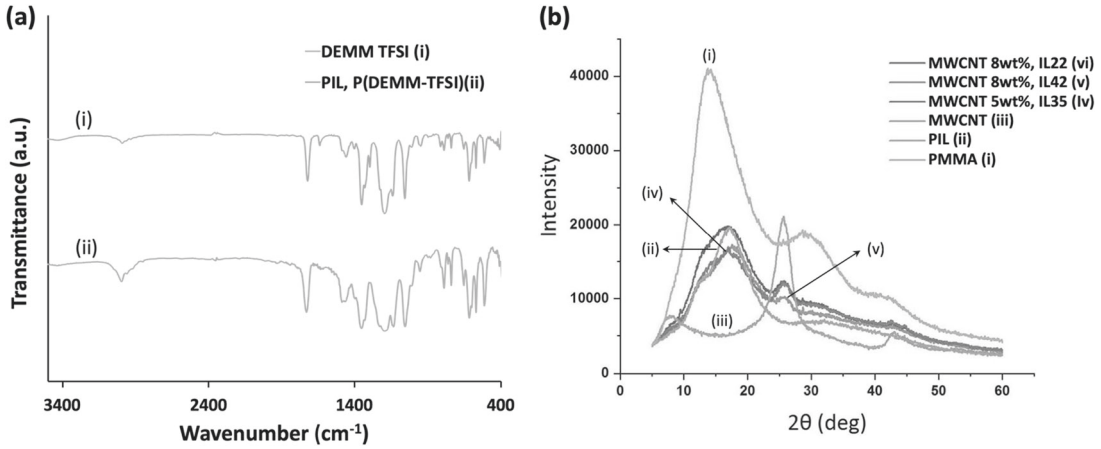

Fig. 3 **a** FTIR spectra of the IL monomer DEMM-TFSI and synthesized PIL, **b** XRD patterns of pristine MWCNTs, PMMA, synthesized PIL, and nanocomposites with different MWCNT and IL contents

1054, 1353 and 1486 cm^{-1}, respectively. A band near 2990 cm^{-1} for the monomer and PIL can be attributed to the C-H stretching vibration of the cationic part.

The X-ray diffraction patterns of the neat PMMA, PIL, MWCNT, and nanocomposite samples are shown in Fig. 3 (b). PMMA is amorphous in nature and exhibits peaks at 2θ values of 13.7 ° and 28.3 ° [38, 39]. For MWCNTs, three peaks at 2θ = 26.6, 43.45, and 54.7 ° are readily observed, which correspond to the (002), (101), and (004) planes, respectively, of the hexagonal graphite structure [40, 41]. The PIL shows amorphous behavior and exhibits a peak at 16.9 °. Nanocomposites with 8 wt.% MWCNTs (IL 22 wt.%, PIL 35 wt.%, and PMMA 35 wt.%), 8 wt.% MWCNTs (IL 42 wt.%, PIL 25 wt.%, and PMMA 25 wt.%), and 15 wt.% CNTs ((IL 35 wt.%, PIL 25 wt.%, and PMMA 25 wt.%) show two dominant peaks, one broad peak in the 2θ region of 14–17 °, mainly attributable to the amorphous PMMA and PIL network, and another peak at 43–44 °, which can be attributed to the MWCNTs within the polymer network. The intensities of the diffraction peaks in the nanocomposites are similar to those of the pristine PIL, signifying the amorphous behavior of the nanocomposites. It is suggested that the IL plays an important role in modifying the crystallinity of the nanocomposites [42]. Nanocomposites with 8 wt.% MWCNTs and different IL contents (22 wt.% and 42 wt.%) show differences in their peak intensities. A high IL content reduces the peak intensity owing to a reduction in the crystallinity of the nanocomposites. Similar observations have been reported elsewhere [42]. In addition, the peaks of the nanocomposites are broader in the presence of the IL.

Mechanical properties

Good mechanical strength and flexibility are prerequisites for any polymer materials utilized in practical applications. The control polymer, i.e., PIL, does not exhibit sufficient mechanical strength or conductivity. The addition of MWCNTs alone to the PIL is not well-suited for 3D-printable filaments because the resulting composites are very brittle. Moreover, the addition of IL to the PIL-MWCNT composites in the absence of PMMA results in paste-like, sticky materials that are very difficult to process both for characterization and 3D printing. PMMA has good compatibility with PDEMM-TFSI, which not only increases the mechanical properties of the nanocomposites but also enhances their processability to a great extent. Among the four components, i.e., PDEMM-TFSI, PMMA, IL DEME TFSI, and MWCNTs, we kept the ratio of PMMA and PDEMM-TFSI at 1:1 with a total content of 50 wt.% (25 wt.%:25 wt.%), and the remaining 50 wt.% was composed of IL and MWCNTs. For example, if the MWCNT content is 7 wt.%, the amount of IL is 43 wt.%. From the stress-strain curves for the tensile tests demonstrated in Fig. 4(a), it can be clearly observed that the composites are very flexible at low MWCNT content, whereas they become more rigid with the increasing MWCNT content. The maximum strain is observed for 7 wt.% and 8 wt.% MWCNT contents, and the maximum stress is observed for 15 wt.% MWCNTs. Thus, Young's moduli, as estimated from the initial slopes of the stress-strain curves, are found to be highest for nanocomposites with 15 wt.% MWCNT and lowest for 7 wt.% MWCNT content (Table 2). It can be noted that the values of Young's moduli are not very high, even at 15 wt.% MWCNT content, signifying the softness of the nanocomposites, which is mainly due to the addition of IL and PIL. Therefore, the mechanical strength and flexibility of the composites can be tuned by the content of MWCNTs, IL, and PIL. The mechanical properties of the PIL-PMMA control and composites with different PMMA: PIL ratios are discussed in the Supplementary Information (Figure S1).

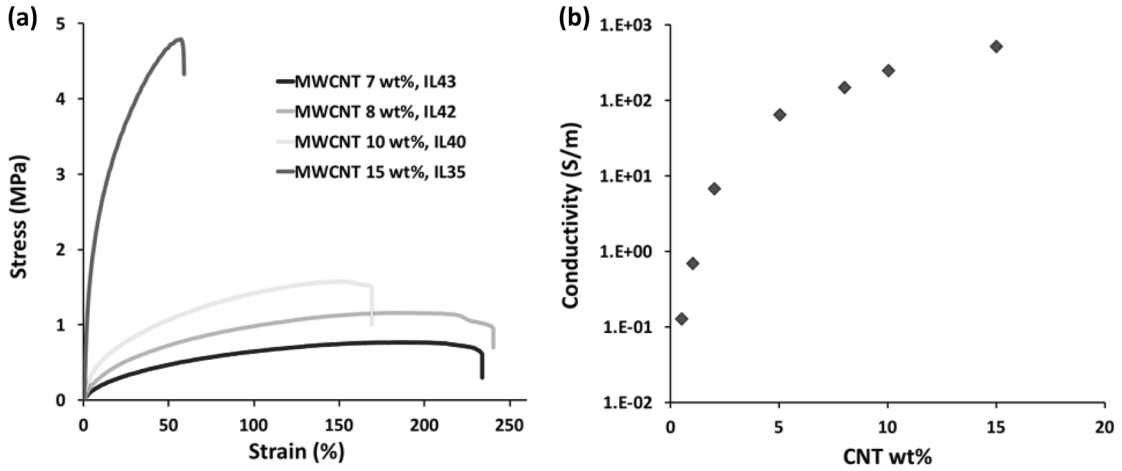

Fig. 4 **a** Representative stress-strain curve from the tensile tests of nanocomposites with different MWCNT contents. **b** conductivity of composites as a function of CNT wt.%

Table 2 Mechanical properties of the nanocomposites

Samples	Young's modulus (MPa)	Stress at break (MPa)	Strain at break (%)
PIL-PMMA control	10^{-5}	n.d.	>3000
MWCNT 7 wt.%, IL43	0.007 ± 0.0004	0.61 ± 0.03	233.92 ± 10.55
MWCNT 8 wt.%, IL42	0.02 ± 0.001	0.91 ± 0.05	240.43 ± 10.65
MWCNT 10 wt.%, IL40	0.07 ± 0.003	1.50 ± 0.07	169.08 ± 7.51
MWCNT 15 wt.%, IL35	2.02 ± 0.12	4.77 ± 0.45	57.58 ± 2.87

n.d. signifies not determined

Conductive properties

The conductive properties of the nanocomposites were measured at r.t. with 0.5–15 wt.% MWCNT content (Fig. 4(b)). PIL-PMMA-IL composites without MWCNTs exhibit conductivities lower than 10^{-6} Sm^{-1}, whereas the addition of MWCNTs at 0.5 wt.% results in a value of 0.12 Sm^{-1}. This value increases exponentially as a function of the MWCNT content. The conductivity of the nanocomposite containing 15 wt.% MWCNTs is 520 Sm^{-1}. It can be mentioned here that the nanocomposites with 0.5–5 wt.% MWCNT contents are very soft due to the high IL content and are difficult to use for 3D printing; however, by increasing the polymeric content (PIL-PMMA), the mechanical strength can be improved. The observed conductivities are some of the highest values that have been reported for MWCNT-doped polymeric IL systems at comparable loadings [16, 30, 43, 44]. The effect of the IL on the conductive properties is discussed in the Supplementary Information (Figure S2), i.e., a noticeable increase in the conductivity similar to the results reported by Zhao et al. [21].

Morphological properties

The morphological structure of the nanocomposites was observed to visualize the dispersion of MWCNTs in the nanocomposite matrix. The morphology of the MWCNTs, PIL-PMMA-IL composite without MWCNTs (PIL-PMMA-IL; 25 wt.%-25 wt.%-50 wt.%), and hot-pressed nanocomposite sheets and extruded filaments was investigated, and their SEM images are shown in Fig. 5. When no polymer is present, the MWCNTs show highly interconnected spaghetti-like networks that have a high tendency to agglomerate with each other. The PIL-PMMA-IL composite without MWCNTs does not show any visible phase separation. However, the presence of different phases is readily observable in the SEM images, and good dispersal of nanocomposites in the IL-rich region is observed for nanocomposites with MWCNT contents of 5, 8 and, 15 wt.%. In the filament cross-sectional image (Fig. 5(f)), the phase containing MWCNTs is found to be more fragmented than that in the film, which might be the extruding effect enhancing the homogeneity of the nanocomposites.

Thermal properties

The thermal decomposition temperatures of PIL and the nanocomposites containing different MWCNT contents were determined and analyzed by TGA. The comparative results of the thermal degradation properties are shown in Fig. 6(a). Pristine PIL shows mainly one-step decomposition with the appearance of a shoulder at 354 °C followed by peak degradation at 392 °C with mass losses of 18 wt.%

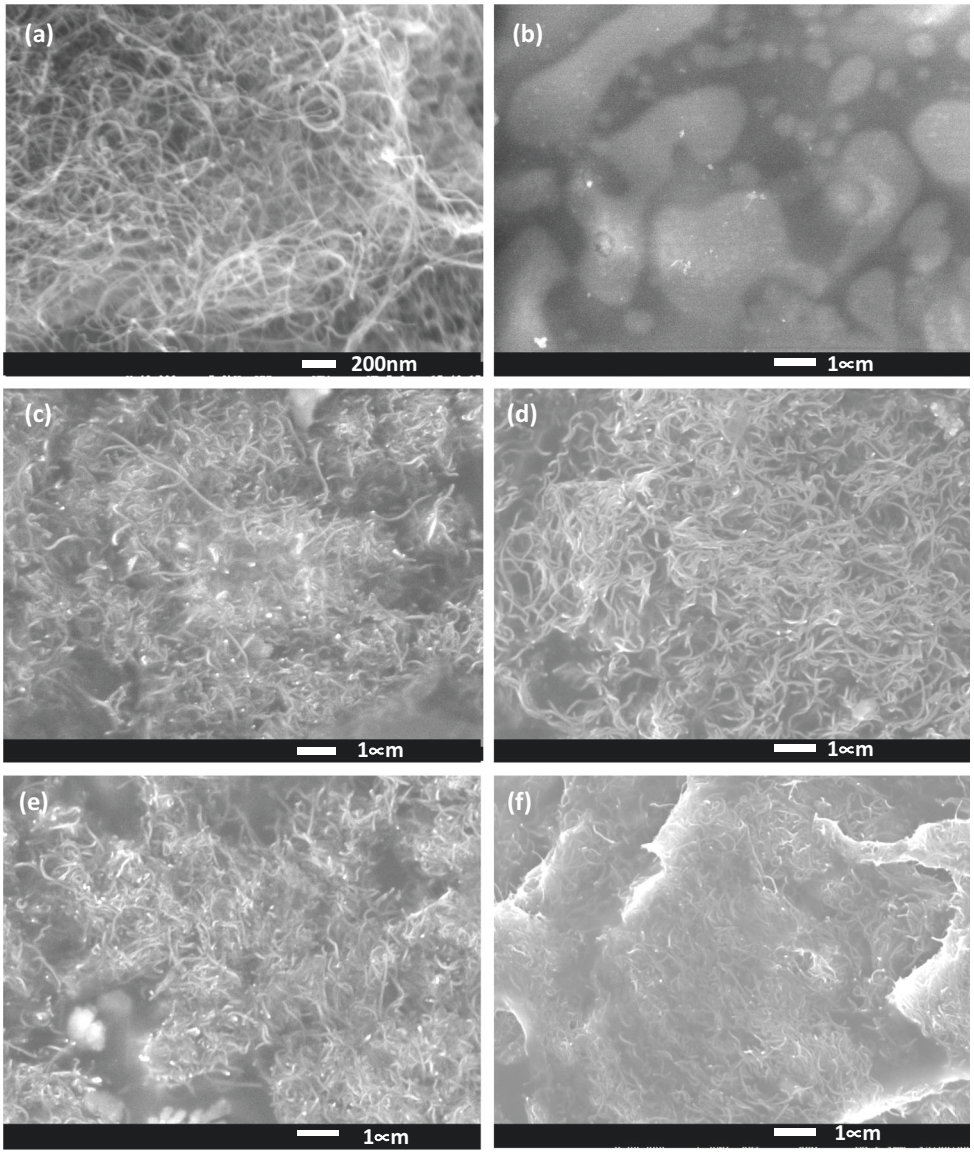

Fig. 5 SEM images of the **a** pristine MWCNTs, **b** PIL-PMMA-IL composite and nanocomposites; **c** MWCNT 5 wt.%, IL45; **d** MWCNT 8 wt. %, IL42; **e** MWCNT 15 wt. %, IL 35 and **f** cross-section of a filament with MWCNT 8wt%, IL42. In all the nanocomposites, the PIL and PMMA wt. ratio is 1:1

and 63 wt.%, respectively. The initial step might have appeared due to the presence of some low-molecular-weight PIL in the total polymer content. MWCNT-containing nanocomposites also exhibit high thermal degradation temperatures similar to those of PIL and demonstrate the trivial effect of the MWCNT content on the degradation temperature of the nanocomposites. However, it can be noted that pristine PIL with no MWCNTs shows a slightly higher thermal stability relative to that of the composites with the mass loss initiating at 340 °C for the 5 wt.% polymer, which is 15 °C higher than that of the nanocomposites at all compositions. The nanocomposites show a well-defined two-step decomposition. The first and second step of decomposition occur between 23–25% weight loss and 68–75% weight loss in the range of 348–353 °C and 406–418 °C, respectively. The first decomposition peak signifies decomposition of PMMA and low-molecular-weight PIL content, whereas the second step implies the degradation temperature of the PIL and IL contents in the polymer matrix. MWCNT fillers are found in the final residue, confirming the MWCNT content in the nanocomposites.

To understand the soft nature of the nanocomposites and to reveal their transition temperature (T_g) from a glass-like state to a rubbery state, we carried out DSC and DMA.

Figure 6(b) shows a DSC thermogram of the PIL, PIL-PMMA control, and nanocomposites with different MWCNT contents. PIL exhibits T_g at 2.0 °C, while the PIL-PMMA control and MWCNT 8 wt.%, IL42 and MWCNT 15 wt.%, IL35 nanocomposites show T_g at −14.2 °C, 1.9 °C, and 4.4 °C, respectively. The T_g value of the PIL-PMMA control decreases due to the plasticizing effect of

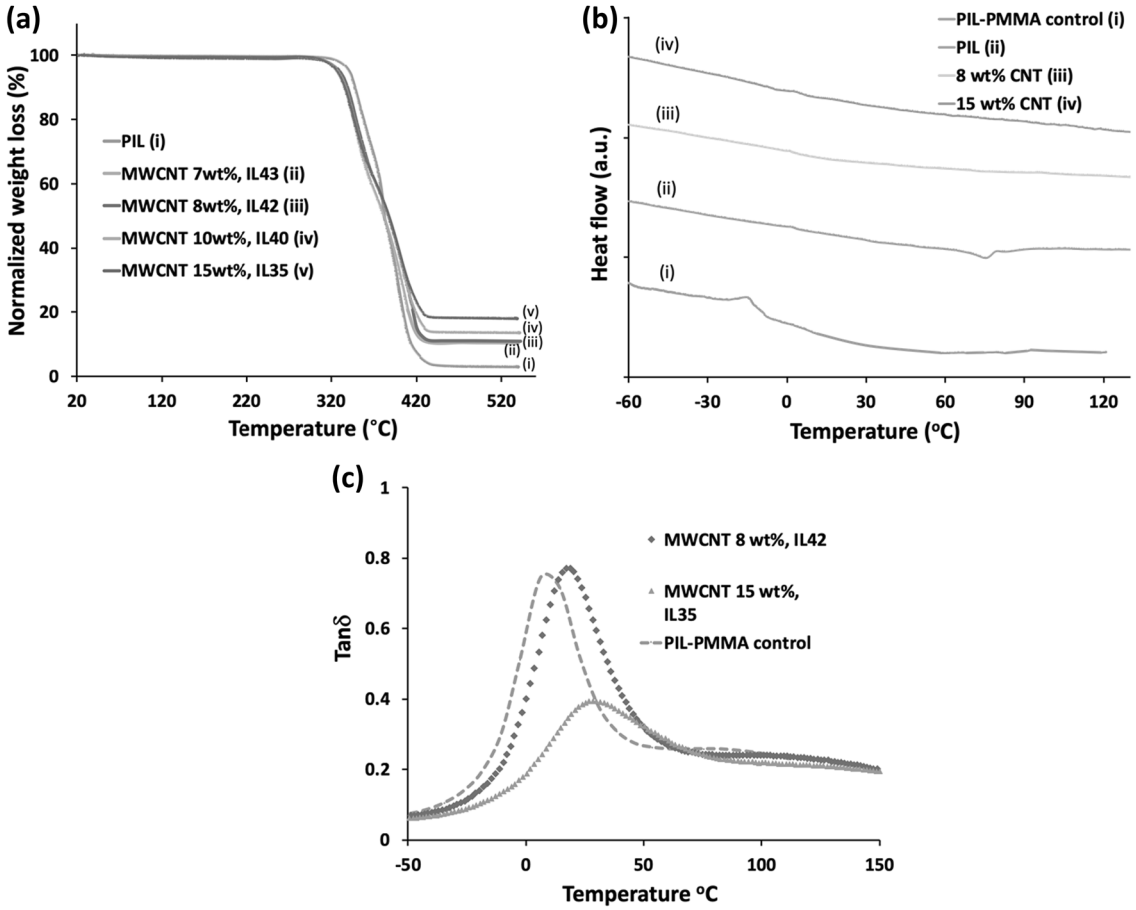

Fig. 6 **a** TGA profile of PIL and nanocomposites with different MWCNT wt.% presenting their degradation, **b** DSC thermogram of PIL and nanocomposites with different MWCNT wt.% and **c** tanδ from DMA as a function of temperature for nanocomposites containing 8 wt.% and 15 wt.% MWCNTs

IL, similar to the phenomenon reported elsewhere [21]. The addition of MWCNTs results in an increase in the T_g value.

The transition was visibly observed by DMA. Figure 6(c) shows the DMA results exhibiting tanδ values as a function of temperature for the PIL nanocomposites, and their storage (E') and loss moduli (E") are presented in the Supplementary Information (Figure S3(a)). The T_g onset for tanδ of the PIL-PMMA control exhibits a peak at 6 °C, while T_g increases with MWCNT filler with T_g onset values of 18 °C and 28 °C for 8 wt.% and 15 wt.% MWCNT contents, respectively. The increase in T_g onset for high filler content can be attributed to the fact that nanocomposites with high MWCNT content enhance rigidity in the polymer matrix, impeding flexibility in the polymer chain at a lower temperature than those with low MWCNT content. It is also worth noting that such a large change in the elastic properties of the material in the transition region is caused by only a small variation in the MWCNT content. The effect of the IL on E' is demonstrated in Figure S3(b) in the Supplementary Information. It is observed that the T_g of the nanocomposites decreases significantly with the IL content, proving their good plasticizing effect. Similar observation has been reported elsewhere [21].

3D-printed multimaterial flexible circuit

The nanocomposites with 8 wt.% CNT loading were used to print different structures, such as mesh and circuit (Fig. 7 (a, b)). A multimaterial flexible circuit board (rectangular shape) consisting of a nanocomposite (8 wt.% MWCNTs, IL 42) circuit path on a commercial flexible polymer matrix (Fabrial^{TM}R, JSR Corporation, Japan) (Fig. 7(b)) was used to demonstrate its practical applicability. For 3D printing, we used the commercial 3D printer MakerBot Replicator 2 with a dual extruder, where one extruder printed the nanocomposites and the other was used for Fabrial^{TM}R. The nozzle diameter of the printer was 0.4 mm, and the extrusion temperature was 200 °C. Printing speed between

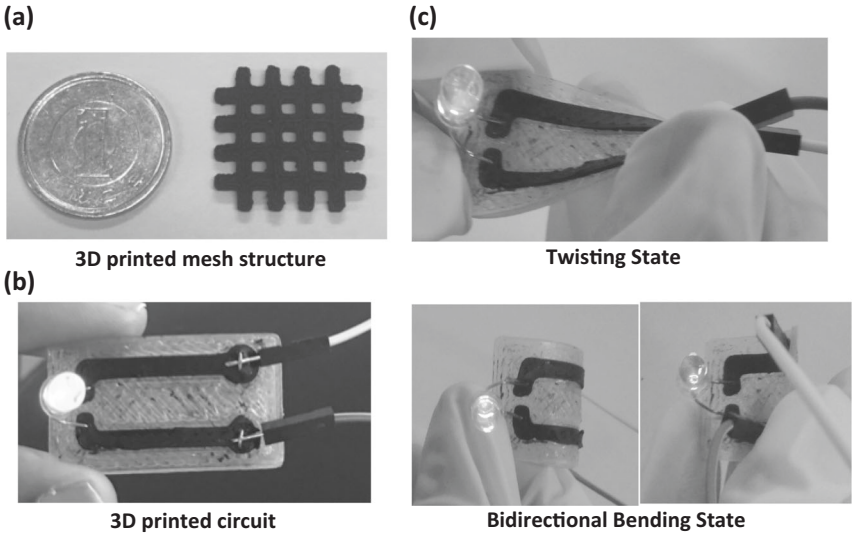

Fig. 7 **a** 3D-printed mesh structure, **b** printed multimaterial flexible circuit where the white base consists of commercially available flexible filament and the black portions consist of nanocomposite filament with 8 wt.% MWCNTs and c demonstration of the LED light operating under twisting and bidirectional bending conditions

600–1200 mm/min was selected with a 0.25 mm layer height for each layer. The size of the rectangular circuit base consisting of Fabrial^{TM}R was 40 mm (height) × 20 mm (width) × 1 or 0.5 mm (thickness) on top of which the nanocomposite circuit path of 1 mm height (four layers) was printed. During printing of the Fabrial^{TM} R matrix, the circuit path was engraved on the matrix at a depth of 0.5 mm, which means that the thickness of the circuit base was 0.5 mm where the nanocomposite line was printed and 1 mm in all other areas. As the attachment between Fabrial^{TM}R and the nanocomposites was not very good, this process enabled physical attachments between the printed nanocomposite circuit and the flexible material. The LED operated at low voltage (3–5 V) under bending and twisting conditions without a disruption in the current flow, as demonstrated in Fig. 7(c). Printed composites consisting of nanocomposite filaments of 8 wt.% MWCNTs with 10 mm length and 2 mm width (thickness 1 mm) show a resistance of ~4 kΩ ± 0.5 kΩ. Some critical conditions were considered during 3D printing, which are discussed in the Supplementary Information. The conductivity of the nanocomposites changes when the circuit is bent or twisted. Such phenomena will be used in the near future to develop 3D-printed sensor devices.

Conclusion

In summary, we have successfully developed a new type of 3D-printable soft polymer nanocompositesnanocomposites utilizing quaternary ammonium cation-based IL and PIL, PMMA, and conductive filler: MWCNT as key components with superior conductivity and tunable ductility. Enhancement of conductive and mechanical properties of the nanocomposites was achieved by increasing the MWCNT content up to 15 wt.%, and the IL content played a significant role in enhancing the flexibility and conductivity of the nanocomposites. Nanocomposites of all compositions possess high thermal stability, and their T_g values lie in the range of 18–28 °C, which was found to be dependent on the MWCNT and IL contents. Finally, we effectively demonstrated the utilization of the nanocomposites by fabricating a flexible and bendable circuit via an FFF printer. Future research work should focus on the effect of other amorphous and crystalline polymers to establish these new industrial materials. We believe that these new materials will create significant progress in developing next-generation 3D-printed robotics, electromechanical sensors, electrochemical systems, and flexible devices that can be easily fabricated in a mold-less and solely automatic process.

Acknowledgements This study was partly supported by the Grant-in-Aid for Scientific Research (Category A, Project No. 17H01224, etc.) from the Japan Society for the Promotion of Science (JSPS), the Centre Of Innovation (COI) program from the Japan Science and Technology Agency (JST), the Strategic Innovation Creation Project (SIP) from the New Energy and Industrial Technology Development Organization (NEDO) of Japan, and the Program on Open Innovation Platform with Enterprises, Research Institute and Academia (OPERA) from the JST. Ahmed K. is supported by the JSPS Fellowship for young scientists in the DC1 category. Authors acknowledge Prof. Tomoya Higashihara`s support for the access to the TGA, DSC, and DMA measurement techniques.

Compliance with ethical standards

Conflict of interest The authors declare that they have no conflict of interest.

References

1. Kalsoom U, Nesterenko PN, Paull B. Recent developments in 3D printable composite materials. RSC Adv. 2016;6:60355–71.
2. Gross BB, Erkal JL, Lockwood SY, Chen C, Spence DM. Evaluation of 3D printing and its potential imapct on biotechnology and chemical science. Anal Chem. 2014;86:3240–53.
3. Muroi H, Hidema R, Gong J, Furukawa H. Development of optical 3d gel printer for fabricating free-form soft & wet industrial materials and evaluation of printed double-network gels. J Solid Mech Mater Eng. 2013;7:163–8.
4. Ahmed K, Naga N, Kawakami M, Furukawa H. Extremely soft, conductive, and transparent ionic gels by 3D optical printing. Macromol Chem Phys. 2018; 1800216. https://doi.org/10.1002/macp.201800216.
5. Shiblee MNI, Ahmed K, Khosla A, Kawakami M, Furukawa H. 3D printing of shape memory hydrogels with tunable mechanical properties. Soft Matter. 2018;14:7809–17.
6. Pham DT, Gault RS. A comparison of rapid prototyping technologies. Int J Mach Tools Manuf. 1998;38:1257–87.
7. Guo S, Gosselin F, Guerin N, Lanouette A, Heuzey MC, Therriault MC. Solvent-cast three-dimensional printing of multifunctional microsystems. Small. 2013;9:4118–22.
8. Farahani R, Lebel L, Therriault D. Processing parameters investigation for the fabrication of self-supported and freeform polymeric microstructures using ultraviolet-assisted three-dimensional printing. J Micromech Microeng. 2014;24:055020.
9. Lebel LL, Aissa B, Khakani MAE, Therriault D. Ultraviolet-assisted direct-write fabrication of carbon nanotube/polymer nanocomposite microcoils. Adv Mater. 2010;22:592–6.
10. Wei X, Li D, Jiang W, Gu Z, Wang X, Zang Z, et al. 3D printable graphene composite. Sci Rep. 2015;5:11181:1-7
11. Guo S, Qiu K, Meng F, Park SH, Mcalpine MC. 3d printed stretchable tactile sensors. Adv Mater. 2017;29:1701218.
12. Muth JT, Vogt DM, Truby RL, Mengüç Y, Kolesky DB, Wood RJ, et al. Embedded 3D printing of strain sensors within highly stretchable elastomers. Adv Mater. 2014;26:6307–12.
13. Guo S, Yang X, Heuzey M, Therriault D. 3D printing of a multifunctional nanocomposite helical liquid sensor. Nanoscale. 2015;7:6451–6.
14. Farahani RD, Chizari K, Therriault D. Three-dimensional printing of freeform helical microstructures: a review. Nanoscale. 2014;6:10470–85.
15. Postiglione G, Natale G, Griffini G, Levi M, Turri S. Conductive 3D microstructures by direct 3D printing of polymer/carbon nanotube nanocomposites via liquid deposition modeling. Compos Part A. 2015;76:110–4.
16. Fukushima T, Kosaka A, Ishimura Y, Yamamoto T, Takigawa T, Ishii N, et al. Molecular ordering of organic molten salts triggered by single-walled carbon nanotubes. Science. 2003;300:2072–4.
17. Fukushima T, Aida T. Ionic liquids for soft functional materials with carbon nanotubes. Chem Eur J. 2007;13:5048–58.
18. Polo-Luque ML, Simonet BM, Valcárcel M. Functionalization and dispersion of carbon nanotubes in ionic liquids. TrAC Trends Anal Chem. 2013;47:99–110.
19. Polo-Luque ML, Simonet BM, Valcárcel M. Solid phase extraction-capillary electrophoresis determination of sulphonamide residues in milk samples by use of C18-carbon nanotubes as hybrid sorbent materials. Analyst . 2013;138:3786–91.
20. Yu P, Zhou H, Zhu N, Lin Y, Mao LA. A facile approach to construction of a stable water-miscible ionic liquid/electrolyte interface with interactions between imidazolium moiety and carbon nanotubes. Electrochem Commun. 2009;11:1393–6.
21. Liping Z, Yongjin L, Xiaojun C, Jichun Y, Wenyong D. Multifunctional role of an ionic liquid in melt-blended poly(methyl methacrylate)/multi-walled carbon nanotube nanocomposites. Nanotechnology. 2012;23:255702.
22. Holbrey JD, Seddon KR. Ionic Liquids. Clean Prod Process. 1999;1:223.
23. Seddon KR. Ionic liquids: a taste of the future. Nat Mater. 2003;2:363–5.
24. Sugino T, Kiyohara K, Takeuchi I, Mukai K, Asaka K. Actuator properties of the complexes composed by carbon nanotube and ionic liquid: the effects of additives. Sens Actuators B. 2009;141:179–86.
25. Terasawa N, Takeuchi I, Matsumoto H, Mukai K, Asaka K. High performance polymer actuator based on carbon nanotube-ionic liquid: effect of ionic liquid. Sens Actuators B. 2011;156:539–45.
26. Nishimura N, Ohno H. 15th anniversary of polymerized ionic liquids. Polym (Guildf). 2014;55:3289–97.
27. Meyer F, Raquez JM, Coulembier O, Winter JD, Gerbaux P, Dubois P. Imidazolium end functionalized poly(L-lactide) for efficient carbon nanotube dispersion. Chem Comm. 2010;46:5527–9.
28. Marcilla R, Curri ML, Cozzoli PD, Martinez MT, Loinaz I, Grande H, et al. Nano-objects on a round trip from water to organics in a polymeric ionic liquid vehicle. Small. 2006;2:507–12.
29. Liu L, Zheng Z, Gu C, Wang X. The poly (urethane-ionic liquid)/multi-walledcarbon nanotubes composites. Compos Sci Technol. 2010;70:1697–703.
30. Fukushima T, Kosaka A, Yamamoto Y, Aimiya T, Notazawa S, Takigawa T, et al. Dramatic effect of dispersed carbon nanotubes on the mechanical and electroconductive properties of polymers derived from ionic liquids. Small. 2006;2:554–60.
31. Bellayer S, Gilman JW, Eidelman N, Bourbigot S, Flambard X, Fox DM, et al. Preparation of homogeneously dispersed multi-walled carbon nanotube/polystyrene nanocomposites via melt extrusion using trialkyl imidazolium compatibilizer. Adv Funct Mater. 2005;15:910–6.
32. Shim Y, Kim HJ. Solvation of carbon nanotubes in a room-temperature ionic liquid. ACS Nano. 2009;3:1693–702.
33. Wang JY, Chu HB, Li Y. Why single walled carbon nanotubes disperse in imidazolium-based ionic liquids. ACS Nano. 2008;2:2540–6.
34. Na S, Singh VK, Singh RK. Development of ion conducting polymer gel electrolyte membranes based on polymer PVdF-HFP, BMIMTFSI ionic liquid and the Li-salt with improved electrical, thermal and structural properties. J Mater Chem C. 2015;3:7305–18.
35. Roy A, Dutta B, Bhattacharya S. Electroactive phase nucleation and non-isothermal crystallization kinetics study in [DEMM][TFSI] ionic liquid incorporated P (VDF-HFP) co-polymer membranes. J Mater Sci. 2016;51:7814–30.
36. Chen X, Zhao J, Zhang J, Qiu L, Xu D, Zhang H, et al. Bis-imidazolium based poly(ionic liquid) electrolytes for quasi-solid-state dye-sensitized solar cells. J Mater Chem. 2012;22:18018–24.
37. Leones R, Costa CM, Machado AV, Esperanc JMSS, Silva MM, Lanceros-Mendez S. Development of solid polymer electrolytes based on poly (vinylidene fluoride-trifluoroethylene) and the [N1112 (OH)][NTf2] ionic liquid for energy storage applications. Solid State Ion. 2013;253:143–50.
38. Stefanescu EA, Tan X, Lin Z, Bowler N, Kessler MR. Multifunctional PMMA-Ceramic Composites as Structural Dielectrics. Polym (Guildf). 2010;51:5823–32.
39. Thakur VK, Vennerberg D, Madboulybc SA, Kessler MR. Bio-inspired green surface functionalization of PMMA for multifunctional capacitors. RSC Adv. 2014;4:6677–84.

40. Xu J, Lv X, Li J, Li Y, Shen L, Zhou H, et al. Simultaneous adsorption and dechlorination of 2,4-dichlorophenol by Pd/Fe nanoparticles with multi-walled carbon nanotube support. J Hazard Mater. 2012;225-6:36–45.
41. Abdel-Ghani NT, El-Chaghaby GA, Helal FS. Individual and competitive adsorption of phenol and nickel onto multiwalled carbon nanotubes. J Adv Res. 2015;6:405–15.
42. Ramesh S, Liew C, Ramesh K. Evaluation and investigation on the effect of ionic liquid onto PMMA-PVC gel polymer blend electrolytes. J Non-Cryst Solids. 2011;357:2132–8.
43. Zhang H, Wang ZG, Zhang ZN, Wu J, Zhang J, He HS. Regenerated cellulose/multiwalled-carbon-nanotube composite fibers with enhanced mechanical properties prepared with the ionic liquid1-allyl-3-methylimidazolium chloride. Adv Mater. 2007;19:698–704.
44. Mandal A, Nandi AK. Ionic liquid integrated multiwalled carbon nanotube in a poly (vinylidene fluoride) matrix: formation of a piezoelectric β-polymorph with significant reinforcement and conductivity improvement. ACS Appl Mater Interfaces. 2013;5:747–60.